Rapid Communications

Quasitopological rotational waves in mechanical granular graphene

Li-Yang Zheng,* Georgios Theocharis, Vincent Tournat, and Vitalyi Gusev†
LAUM, UMR-CNRS 6613, Le Mans Université, Avenue O. Messiaen, 72085 Le Mans, France

(Received 21 July 2017; published 22 February 2018)

Granular crystals are periodic structures of elastic beads arranged in crystal lattices. One important feature of granular crystals is that the interactions between beads can take place via noncentral contact forces, leading to the propagation of rotational and coupled rotational-translational waves. Here, we theoretically demonstrate the topological properties of these mechanical rotational waves in a granular graphene, a two-dimensional monolayer honeycomb granular crystal with Dirac dispersion at the center of the Brillouin zone. Around the Dirac point, effective spin, helicity, and effective spin-orbit coupling are illustrated in the mechanical granular system. Finally, quasitopological transport, where the rotational edge waves are nearly topologically protected, is observed on the interface.

DOI: 10.1103/PhysRevB.97.060101

Recently, the study of topology in materials/metastructures has attracted increasing attention [1–12]. One of the fascinating features of those materials is that boundaries or interfaces support the topological transport of edge waves that are immune to backscattering when traveling through defects. Such an appealing property has inspired the development of various types of schemes with topological phases in photonic and phononic systems. On the one hand, in analogy with the quantum Hall effect, topological transport can be achieved by breaking the time-reversal symmetry. Examples include photonic crystals with a magnetic field [13], and phononic crystals with circulating fluids [14]. On the other hand, based on the idea of the quantum spin Hall effect (QSHE), topological wave propagation in the presence of time-reversal symmetry (TRS) also has been proposed [15–24]. In this case, a pair of spin-polarized edge states appear on the boundary/interface, giving rise to a topological insulator of Z_2 category [15–17]. Several approaches to Z_2 topological insulator analogies in optics, acoustics, and elastodynamics have been exploited, including bianisotropic photonic crystals [18,19], photonic/phononic crystals with a pseudo-time-reversal symmetry [20–23], and elastic metamaterials with effective spin-orbit coupling (SOC) [24].

There also has been a growing interest in investigating the topology in discrete mechanical spring-mass systems [25–30]. Examples include metamaterials with rotating gyroscopes [25,26], mechanical structures subjected to a Coriolis force caused by permanent rotation of the system [27], and coupled pendula systems exhibiting QSHE [28]. In those proposals, the systems either require an external rotating bias to break time-reversal symmetry [25–27] or need to be sophisticatedly designed in order to induce couplings between pendula [28]. In addition, the role of rotational degrees of freedom of individual masses has seldom been evaluated [29]. Due to the existence of noncentral forces, which can initiate the rotation of individual mass particles, rotations become crucial in wave propagation in discrete mechanical systems [31,32]. Especially in granular crystals, the interactions between beads can take place via transverse rigidities of contacts [31–41], leading to the propagation of rotational elastic waves. Previous investigations have theoretically and experimentally revealed the existence of rotational-translational bulk waves [33–36], rotational edge/surface waves [37,38], etc. Therefore, the rotation of individual particles should be taken into account when exploiting the topological order in granular crystals.

In this Rapid Communication, we study the topological properties of rotational edge waves in a granular graphene (GG) with TRS. It has been reported that a topological wave effect can be achieved with TRS in analogy to the quantum valley Hall effect [10,11,30], whereas our strategy is based on an analogy with QSHE. The GG, a honeycomb granular monolayer consisting of three-dimensional (3D) elastic particles, is shown in Fig. 1(a). Although the beads are 3D in nature, the dynamics in the structure is two dimensional (2D). We consider the out-of-plane motion, which activates in-plane rotations with angles φ,ϕ relative to the axes in the x and y directions, respectively, and the out-of-plane displacement u along the z axis [Fig. 1(b)]. The movements of individual particles can induce three types of forces and/or moments between the particles [36,37]: (1) transverse forces controlled by an effective shear rigidity ξ_s [Fig. 1(c)], (2) torsional forces characterized by an effective torsional rigidity ξ_t [Fig. 1(d)], and (3) bending forces characterized by an effective bending rigidity ξ_b [Fig. 1(e)]. By analyzing the motions in one unit cell and the interactions with its neighbors, the dynamical equation of bulk waves is given by

$$\mathcal{D}\boldsymbol{v} = \Omega^2 \boldsymbol{v}, \tag{1}$$

where $\Omega = \omega\sqrt{M/\xi_s}$ is the normalized frequency, ω is the cyclic frequency, M is the mass of particles, and $\boldsymbol{v} = [u_A; \Phi_A; \Psi_A; u_B; \Phi_B; \Psi_B]$ with $\Phi = R\varphi$, $\Psi = R\phi$ (R is the radius of particles). $\mathcal{D}$ is a 6×6 dynamical matrix [42]. Equation (1) gives the $\Omega - k$ dispersion relation, which is controlled by three parameters, the factor $\mathrm{P} = MR^2/I$ (I is the inertia of beads) and the normalized bending and

*liyang.zheng.etu@univ-lemans.fr
†vitali.goussev@univ-lemans.fr

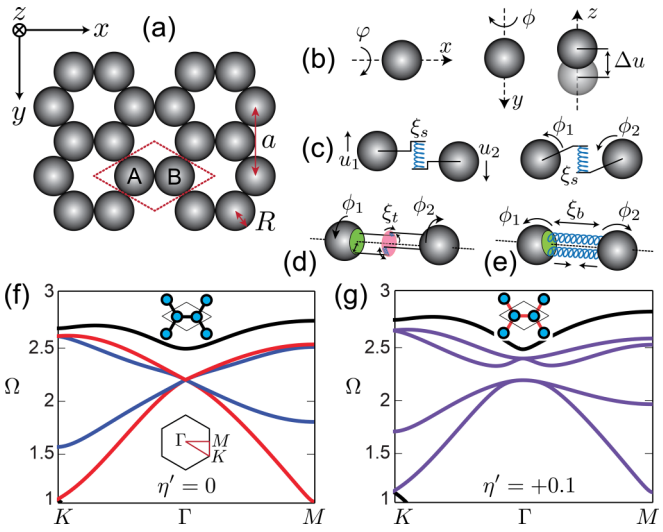

FIG. 1. (a) Granular graphene: The red dashed box marks the unit cell containing two particles, A and B. Movements of individual particles in (b) can generate shear forces (c), torsional forces (d), and bending forces (e). The band structures for $\eta_b = \eta_t = 0.5$ and $\mathrm{P} = 1.55$ are shown when perturbation $\eta' = 0$ in (f) and $\eta' = +0.1$ in (g). The red branches in (f) are dominated by $\boldsymbol{d}$ modes, and the blue ones by $\boldsymbol{p}$ modes. The black (red) bonds in the insets of (f) [(g)] indicate that the bending and torsional rigidities between particles are unmodified (modified).

torsional rigidities $\eta_{b,t} = \xi_{b,t}/\xi_s$. The existence of topological edge waves preserving TRS requires a degenerate Dirac cone (double Dirac cone) in the absence of perturbation and a complete band gap in the presence of perturbation [24]. Thus, we analyze the GG with $\mathrm{P} = 1.55$ and $\eta_b = \eta_t = 0.5$. The dispersion is shown in Fig. 1(f), where a double Dirac cone appears at the Dirac frequency $\Omega_D = \sqrt{3}\mathrm{P}$ in the center of the Brillouin zone (BZ). Adding a perturbation η' to η_b and η_t, the Dirac cone disappears and a complete band gap appears. Figure 1(g) shows the case when η_b and η_t are perturbed by $\eta' = +0.1$, namely, $\eta_b = \eta_t = 0.6$.

Due to the existence of noncentral transverse forces, rotational-translational coupled modes exist in the GG. However, around the Dirac point, the blue and red branches support modes dominated by rotation. The contribution of translation (u components) is very small compared to the rotational ones [42]. This allows us to approximate the 6×6 eigenvalue problem by a 4×4 one in the vicinity of the Dirac point (at Γ point), namely, for a small wave vector $\Delta\boldsymbol{k} = (\Delta k_x, \Delta k_y)$ and for $\Delta\Omega \ll \Omega_D$. In addition, we alter the original basis into the circular polarized basis $\boldsymbol{p} = [p_\uparrow; ip_\downarrow] = [\Phi_A + i\Psi_A; i(\Phi_B - i\Psi_B)]/\sqrt{2}$ and $\boldsymbol{d} = [d_\uparrow; id_\downarrow] = [-(\Phi_B + i\Psi_B); i(\Phi_A - i\Psi_A)]/\sqrt{2}$, where "↑↓" denote the left/right circular polarizations. As shown in Fig. 2(a), under the new basis, the GG exhibits a pair of "spin" states in the mechanical system which physically are the rotations of a particle with left/right circular polarizations (the rotation vector is circulating left/right handed with time). In the vicinity of the Dirac point, Eq. (1) can be approximated by the following equation,

$$\begin{bmatrix} H(\Delta\boldsymbol{k}) & m\sigma_z \\ m\sigma_z & H(\Delta\boldsymbol{k}) \end{bmatrix} \boldsymbol{\psi}(\Delta\boldsymbol{k}) = \delta\Omega\boldsymbol{\psi}(\Delta\boldsymbol{k}), \tag{2}$$

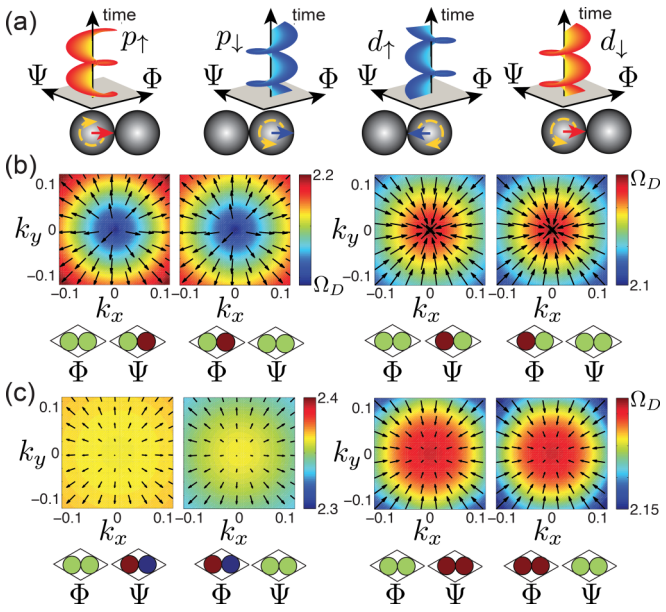

FIG. 2. (a) Possible mechanical spin states in the GG. The left (right) circular polarization of rotation is the spin ↑ (↓) state. The red (blue) arrow represents the rotation vector of particle A (B). Projection of helical modes with perturbation (b) $\eta' = 0$ and (c) $\eta' = 0.1$ on $\boldsymbol{k}$ space. The arrow denotes the axis of spin projection. The "currents" in the upper branches are outgoing (right handed) while in the lower branches they are incoming (left handed). The color in the background represents the eigenfrequency. The eigenmodes of the Γ point are also shown in (b) when $\eta' = 0$ and in (c) when $\eta' = 0.1$.

where $m = \eta'\Omega_D/2$ denotes the "effective mass" due to perturbation η', $\delta\Omega = \Omega - \Omega_D - m$, $H(\Delta\boldsymbol{k}) = V_D\boldsymbol{\sigma}\cdot\Delta\boldsymbol{k}$ is a 2×2 Dirac Hamiltonian with the Dirac velocity $V_D = \Omega_D R/4$ and the Pauli matrices $\boldsymbol{\sigma} = (\sigma_x, \sigma_y, \sigma_z)$, while the four-component spinor $\boldsymbol{\psi}(\Delta\boldsymbol{k})$ is composed of the two-component spinors $\boldsymbol{p}, \boldsymbol{d}$, namely, $\boldsymbol{\psi} = [\boldsymbol{p}; \boldsymbol{d}]$. In the absence of perturbation, $\eta' = 0$, the zero off-diagonal blocks in Eq. (2) suggest that the $\boldsymbol{p}$ and $\boldsymbol{d}$ spinors are uncoupled. Consequently, the double Dirac cone is the degeneracy of the Dirac cones of $\boldsymbol{p}$ (blue lines) and $\boldsymbol{d}$ (red lines) spinor subsystems at the Dirac frequency Ω_D, as marked in Fig. 1(f). It is worth noting that the effective Hamiltonian of 2D Dirac matter [43] in Eq. (2) can be also derived from the band theory of electronic topological insulators [15–17].

It is clear that the presence of perturbation induces hybridization between the $\boldsymbol{p}$ and $\boldsymbol{d}$ spinors. To simplify further Eq. (2), we can diagonalize it by an appropriate unitary transformation [42]. Under the new spinor $\boldsymbol{\psi'} = [S_+^\uparrow; S_+^\downarrow; S_-^\uparrow; S_-^\downarrow] = [p_\uparrow + d_\uparrow; i(p_\downarrow + d_\downarrow); p_\uparrow - d_\uparrow; i(p_\downarrow - d_\downarrow)]/\sqrt{2}$, Eq. (2) can be rewritten as two decoupled equations $\mathcal{H}_\pm(\Delta\boldsymbol{k})\boldsymbol{S}_\pm = \delta\Omega\boldsymbol{S}_\pm$ with the Hamiltonian,

$$\mathcal{H}_\pm(\Delta\boldsymbol{k}) = V_D\boldsymbol{\sigma}\cdot\Delta\boldsymbol{k} \pm m\sigma_z. \tag{3}$$

The second term in Eq. (3) describes the hybridization of $\boldsymbol{p}$ and $\boldsymbol{d}$ spinor subsystems, which can be regarded as the effective spin-orbit coupling in the GG. The signs "±" determine the nature of the eigenmodes to be $\boldsymbol{S}_+$ or $\boldsymbol{S}_-$ types. $\mathcal{H}_\pm$ predicts the helicity-locking property of the bulk modes. The helicity in this mechanical system is defined as $\widehat{h} = \boldsymbol{\sigma}\cdot\boldsymbol{e}$ ($\widehat{h}$ commutes with $\mathcal{H}_\pm$) with a unit vector $\boldsymbol{e} = (V_D\Delta k_x/\lambda, V_D\Delta k_y/\lambda, m/\lambda)$

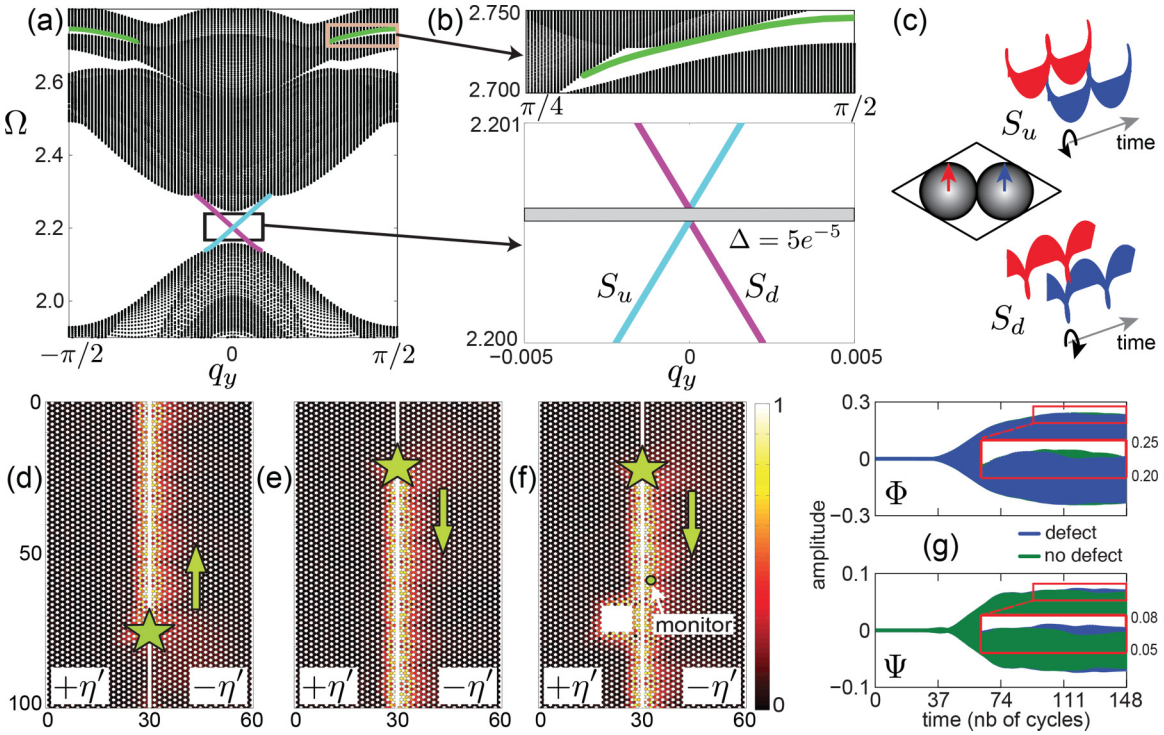

FIG. 3. (a) Dispersion of the edge wave along the y direction. The gray lines correspond to the bulk modes and color lines to the edge modes. (b) Zooms of different edge branches. The green lines represent topologically trivial edge modes. (c) Schematics to reveal the spin nature of modes in the cyan and magenta branches in (b). The arrow in red (blue) in the unit cell represents the rotation direction of particle A (B). Time evolution simulations for the S_u edge wave in (d) and the S_d edge wave in (e). The green stars highlight the positions of source. (f) The same configuration as (c) except that there is a hole close to the interface. The color scale is the magnitude of the total rotation normalized to the maximum. The movement of a bead marked by the circle is monitored to compare with the case in (e). (g) Rotation signals at the monitored bead.

and $\lambda = \sqrt{V_D^2 \Delta \boldsymbol{k}^2 + m^2}$. The helicity matrix $\widehat{h}$ gives two eigenvalues ± 1, which determine the eigenmodes to be right-handed $(+1)$ or left-handed (-1) helical states [42]. For right-handed helical states, the helicity is aligned in the same direction as $\boldsymbol{e}$, while it is the opposite for the left-handed helical states. Thus, the directions of the helicity vectors are given by $(\pm V_D \Delta k_x/\lambda, \pm V_D \Delta k_y/\lambda, \pm m/\lambda)$ for the right-handed and left-handed helical states, respectively. The helicity patterns (namely, the projection of the helicity in $\boldsymbol{k}$ space) of the eigenmodes around the Γ point in the upper and lower $\boldsymbol{S}_\pm$ branches are shown by arrows in Figs. 2(b) and 2(c). In the absence of perturbation, $\eta' = 0$, the arrows keep the same length, as shown in Fig. 2(b). The upper Dirac cones support the right-handed helical modes, exhibiting the outgoing "currents" [left of Fig. 2(b)], while the lower Dirac cones support the left-handed helical modes, showing the incoming "currents" [right of Fig. 2(b)]. In the presence of perturbation, $\eta' = +0.1$, as depicted in Fig. 2(c), the "currents" of the upper and lower branches remain in patterns similar to those of the unperturbed case, while the lengths of the arrows become shorter when approaching the Γ point. At the Γ point, the in-plane arrows vanish, indicating a vector $\boldsymbol{e}$ pointing exactly along the z axis. The eigenmodes of the Γ point are also shown in Fig. 2(b) when $\eta' = 0$ and in Fig. 2(c) when $\eta' = +0.1$. It shows that the eigenmodes in Fig. 2(c) are the combinations of the ones in Fig. 2(b), confirming the existence of hybridization of the $\boldsymbol{p}$ and $\boldsymbol{d}$ states.

The GG, with the effective Hamiltonian $\mathcal{H}_\pm$, is expected to exhibit a nonzero Z_2 topological invariant. We found that the spin Chern number around the Γ point is ± 1 for the rotational branches in Fig. 1(g), confirming the nontrivial topology of the bands [42]. Therefore, it is possible to observe a pair of topological edge waves on the interface by combining two GGs with $\eta' = \pm 0.1$. On the interface, the bonds connecting the left and right GGs are not modified. To ensure that the two GGs exhibit overlapping gaps, the mass of beads of the right GG has been scaled down by a factor $f = 0.92$. The dispersion curves in Fig. 3(a) confirm the existence of a pair of rotational edge waves in the gap. The gray lines correspond to the bulk modes which are projected to the $q_y = \sqrt{3} k_y R$ direction. The cyan (magenta) lines correspond to upward S_u (downward S_d) propagating rotational edge waves. The green lines mark the topologically trivial branches of the edge wave. The time evolutions of the eigenmodes of the edge waves with opposite signs of k_y are implemented in Fig. 3(c), where a unit cell of the interface is shown. The arrow in red (blue) represents the rotation direction of particle A (B), which is circulating with increasing time. The rotation trajectories of the red and blue arrows suggest that the edge modes on the cyan (magenta) branches are left (right) circularly polarized. Therefore, the cyan/magenta branches (S_u/S_d modes) support the propagation of rotational edge waves with different polarizations. The spatiotemporal evolution simulations of edge waves are shown in Figs. 3(d) and 3(e), and an interface unit cell is used to be

the source (star) to excite the harmonic edge wave $A_{\pm}e^{-i\omega t}$, where $A_{\pm}$ are the eigenmodes of S_u and S_d waves [42]. In Figs. 3(d) and 3(e), upward S_u and downward S_d propagating rotational edge waves are observed, manifesting the one-way propagation property of the rotational edge wave.

It should be mentioned that only when the edge wave is gapless can topological transport exist on the interface, where a pair of spin-polarized edge waves are preserved. However, the dispersion of the edge waves in the GG is not gapless as there is a tiny gap [Fig. 3(b)]. The existence of a tiny gap can lead to the coupling of spin-polarized helical edge states, resulting in the hybridized S_u and S_d rotational edge waves to be nonperfectly topologically protected. This is confirmed by the spatiotemporal evolution simulations in Fig. 3(f), where the interface configuration is identical to Fig. 3(e), except that a hole is placed close to the interface. We monitor the particle at the position marked by the circle to see if there is backreflection. The rotational movements of the particle as a function of time are shown in Fig. 3(g) both for the cases with and without the hole. The difference in the two cases shows that reflection is measured after a certain time, suggesting that the edge wave is nonperfectly immune to backscattering when defects are introduced.

The origin of this tiny gap can be physically explained by analyzing the interface dynamics [42]. When $f \neq 1$, the changing of the masses on one side of the interface causes coupling of the two spin-polarized helical edge states, resulting in a gap for the edge wave. When defects appear, the spin-polarized states can flip to the others, turning the edge waves from being perfectly immune to being nonperfectly immune to defects. Consequently, backscattering can be detected as shown in Fig. 3(g). However, as can be seen in Fig. 3(b), the width of the tiny gap is $\Delta = 5e^{-5}$ when $f = 0.92$, suggesting that the hybridization of the spin-polarized helical edge states is very weak. Therefore, the backscattering is too small, and the propagation of rotational edge waves can be regarded as quasitopologically protected. The rotational edge waves in the GG are still quite robust against defects. As an example, in Fig. 4(a), a zigzag path with two corners is constructed. The same source (star) as in Fig. 3(e) is applied to launch the S_d edge wave. It can be seen that the S_d wave can turn the corners and keep propagating without noticeable backscattering. For comparison, in Fig. 4(b), a normal edge wave with $q_k = \pi/3$ in the green branch of Fig. 3(b) is excited from the same position as Fig. 4(a), showing clearly reflections and diffractions when the wave meets the corner and no output rotational edge wave in the end.

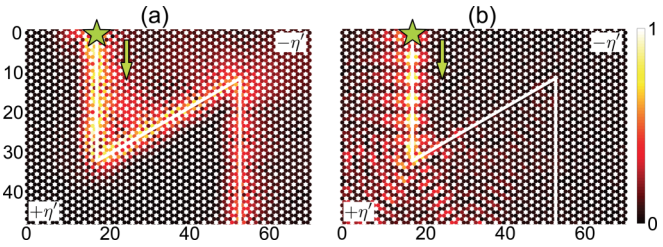

FIG. 4. Robustness of the quasitopological rotational wave against defects: a zigzag path containing two corners. (a) S_d edge wave is launched from the position marked by the green star. For comparison, a normal edge wave is excited from the same positions in (b).

In conclusion, the topological properties of rotational edge waves in a GG in a similar way to the QSHE have been demonstrated. The mechanical spin, helicity, and the effective SOC are illustrated in the GG. Quasitopological transport is observed on an interface constructed by two GGs with different stiffnesses and masses of particles. The easy construction of granular crystals, combined with other features such as tunability upon external fields/mechanical loading and an enhanced nonlinear response, make them a perfect testbed for further fundamental studies in the field of topological mechanics.

This work was supported by a fellowship of the China Scholarship Council for L.-Y.Z., the project Pari Scientifique PROPASYM funded by Region Pays-de-la-Loire, and the FP7-CIG Project No. 618322 ComGranSol.

[1] M. Z. Hasan and C. L. Kane, Rev. Mod. Phys. **82**, 3045 (2010).
[2] X.-L. Qi and S.-C. Zhang, Rev. Mod. Phys. **83**, 1057 (2011).
[3] M. Hafezi, E. A. Demler, M. D. Lukin, and J. M. Taylor, Nat. Phys. **7**, 907 (2011).
[4] L. Lu, J. D. Joannopoulos, and M. Soljacic, Nat. Photonics **8**, 821 (2014).
[5] G. Q. Liang and Y. D. Chong, Phys. Rev. Lett. **110**, 203904 (2013).
[6] M. C. Rechtsman, J. M. Zeuner, Y. Plotnik, Y. Lumer, D. Podolsky, F. Dreisow, S. Nolte, M. Segev, and A. Szameit, Nature (London) **496**, 196 (2013).
[7] W.-J. Chen, S.-J. Jiang, X.-D. Chen, B. Zhu, L. Zhou, J.-W. Dong, and C. T. Chan, Nat. Commun. **5**, 5782 (2014).
[8] C. L. Kane and T. C. Lubensky, Nat. Phys. **10**, 39 (2014).
[9] J. Paulose, B. G. Chen, and V. Vitelli, Nat. Phys. **11**, 153 (2015).
[10] J. Lu, C. Qiu, M. Ke, and Z. Liu, Phys. Rev. Lett. **116**, 093901 (2016).
[11] J.-W. Dong, X.-D. Chen, H. Zhu, Y. Wang, and X. Zhang, Nat. Mater. **16**, 298 (2017).
[12] R. Fleury, A. B. Khanikaev, and A. Alu, Nat. Commun. **7**, 11744 (2016).
[13] Z. Wang, Y. Chong, J. D. Joannopoulos, and M. Soljacic, Nature (London) **461**, 772 (2009).
[14] Z. Yang, F. Gao, X. Shi, X. Lin, Z. Gao, Y. Chong, and B. Zhang, Phys. Rev. Lett. **114**, 114301 (2015).
[15] C. L. Kane and E. J. Mele, Phys. Rev. Lett. **95**, 226801 (2005).
[16] C. L. Kane and E. J. Mele, Phys. Rev. Lett. **95**, 146802 (2005).
[17] B. A. Bernevig, T. L. Hughes, and S.-C. Zhang, Science **314**, 1757 (2006).
[18] A. B. Khanikaev, S. H. Mousavi, W.-K. Tse, M. Kargarian, A. H. MacDonald, and G. Shvets, Nat. Mater. **12**, 233 (2013).
[19] T. Ma, A. B. Khanikaev, S. H. Mousavi, and G. Shvets, Phys. Rev. Lett. **114**, 127401 (2015).
[20] L.-H. Wu and X. Hu, Phys. Rev. Lett. **114**, 223901 (2015).

[21] C. He, X.-C. Sun, X.-P. Liu, M.-H. Lu, Y. Chen. L. Feng, and Y.-F. Chen, Proc. Natl. Acad. Sci. USA **113**, 4924 (2016).
[22] C. He, X. Ni, H. Ge, X.-C. Sun, Y.-B. Chen, M.-H. Lu, X.-P. Liu, and Y.-F. Chen, Nat. Phys. **12**, 1124 (2016).
[23] J. Mei, Z. Chen, and Y. Wu, Sci. Rep. **6**, 32752 (2016).
[24] S. H. Mousavi, A. B. Khanikaev, and Z. Wang, Nat. Commun. **6**, 8682 (2015).
[25] L. M. Nash, D. Kleckner, A. Read, V. Vitelli, A. M. Turnerc, and W. T. M. Irvine, Proc. Natl. Acad. Sci. USA **112**, 14495 (2015).
[26] P. Wang, L. Lu, and K. Bertoldi, Phys. Rev. Lett. **115**, 104302 (2015).
[27] Y.-T. Wang, P.-G. Luan, and S. Zhang, New J. Phys. **17**, 073031 (2015).
[28] R. Süsstrunk and S. D. Huber, Science **349**, 47 (2015).
[29] P. A. Deymier, K. Runge, N. Swinteck, and K. Muralidharan, C. R. Mec. **343**, 700 (2015).
[30] R. K. Pal and M. Ruzzene, New J. Phys. **19**, 025001 (2017).
[31] A. S. J. Suiker, A. V. Metrikine, and R. de Borst, Int. J. Solids Struct. **38**, 1563 (2001).
[32] L. M. Schwartz, D. L. Johnson, and S. Feng, Phys. Rev. Lett. **52**, 831 (1984).
[33] V. Tournat, I. Perez-Arjona, A. Merkel, V. Sanchez-Morcillo, and V. Gusev, New J. Phys. **13**, 073042 (2011).
[34] A. Merkel, V. Tournat, and V. Gusev, Phys. Rev. Lett. **107**, 225502 (2011).
[35] F. Allein, V. Tournat, V. E. Gusev, and G. Theocharis, Appl. Phys. Lett. **108**, 161903 (2016).
[36] L.-Y. Zheng, H. Pichard, V. Tournat, G. Theocharis, and V. Gusev, Ultrasonics **69**, 201 (2016).
[37] L.-Y. Zheng, V. Tournat, and V. Gusev, Extreme Mech. Lett. **12**, 55 (2017).
[38] M. Hiraiwa, M. Abi Ghanem, S. P. Wallen, A. Khanolkar, A. A. Maznev, and N. Boechler, Phys. Rev. Lett. **116**, 198001 (2016).
[39] N. Boechler, J. K. Eliason, A. Kumar, A. A. Maznev, K. A. Nelson, and N. Fang, Phys. Rev. Lett. **111**, 036103 (2013).
[40] N. Boechler, G. Theocharis, and C. Daraio, Nat. Mater. **10**, 665 (2011).
[41] F. Li, P. Anzel, J. Yang, P. G. Kevrekidis, and C. Daraio, Nat. Commun. **5**, 5311 (2014).
[42] See Supplemental Material at http://link.aps.org/supplemental/10.1103/PhysRevB.97.060101 for discussions on symmetry, wave dynamics around the Dirac point, numerical method, and generalizations.
[43] G. Tkachov, *Topological Insulators: The Physics of Spin Helicity in Quantum Transport* (Taylor and Francis, London, 2016).